Precambrian Research 300 (2017) 261–272

Contents lists available at ScienceDirect

Precambrian Research

journal homepage: www.elsevier.com/locate/precamres

Crustal structure of southern Burkina Faso inferred from magnetotelluric, gravity and magnetic data

F. Le Pape[a,*], A.G. Jones[a,1], M.W. Jessell[b,e], S. Perrouty[c], L.A. Gallardo[d], L. Baratoux[e,f], C. Hogg[a], L. Siebenaller[e], A. Touré[g], P. Ouiya[h], G. Boren[i]

[a] Dublin Institute for Advanced Studies, Ireland
[b] Centre for Exploration Targeting, The University of Western Australia, Australia
[c] Western University, Earth Sciences, London, ON, Canada
[d] Earth Science Division, Centro de Investigación Científica y de Educación Superior de Ensenada, B.C., Mexico
[e] Université de Toulouse, CNRS, Géosciences Environnement Toulouse, Institut de Recherche pour le Développement, Observatoire Midi-Pyrénées, Toulouse, France
[f] IFAN Cheikh Anta Diop, Dakar, Senegal
[g] BUMIGEB, Burkina Faso
[h] University of Ouagadougou, Burkina Faso
[i] University of Adelaide, Australia

ARTICLE INFO

Keywords:
West African craton
Burkina Faso
Magnetotellurics
Gravity
Magnetization
Joint inversion

ABSTRACT

Understanding the architecture of the West African craton at depth is essential to be able to reconstruct its evolution. Our study focuses on the crustal imaging of structures and geometries characterizing the crust of the Leo-Man shield with broadband and long period magnetotelluric data collected in southern Burkina Faso and covering a 220 km long profile. The resulting 3D resistivity crustal model highlights the distribution of the granite-greenstone assemblages with depth showing excellent correlation with mapped surficial lithologies. The whole crust of southern Burkina Faso is resistive, with lateral as opposed to vertical major resistivity contrasts, reflecting the location of major-scale shear zones characterizing this part of the Baoulé-Mossi domain. Ground gravity data acquired along the same line as the MT data were also modeled and show relatively good correspondence with the resistivity model. The new resistivity and gravity models compared with results from joint inversion of gravity and aeromagnetic data highlight significant changes between the greenstone belts and granitoid domains along the profile. The comparison of the geophysics with the geology enables us to define new depth constraints of the main tectonic features in the area. The observed large scale dipping shear zones favour the model of crustal building through major parallel thrust faults.

1. Introduction

The Leo-Man Shield hosts the Paleoproterozoic lithologies that bound the main Archean nucleus of the southeastern part of the West African craton. The Baoulé-Mossi domain forms the eastern and northern parts of the Leo-Man Craton (Bessoles, 1977) and reflects typical Archean-like greenstone-granitoid assemblages consisting of Birimian volcano-sedimentary belts separated by extensive tonalite-trondhjemite-granodiorite and granitoid provinces (Baratoux et al., 2011). Two distinct tectonic models have been proposed to explain the tectonic evolution of the granite-greenstone domains. The first model invokes a plate tectonics scenario where crustal building involves major parallel thrust faults (Hirdes et al., 1996; Feybesse et al., 2006; Baratoux et al., 2011). In contrast, the second model explains the granite-greenstone formations as a result of vertical motion, or sagduction, related to gravitational instabilities (Pons et al., 1995; Vidal et al., 2009; Lompo, 2010). Due to a thick lateritic cover, the Paleoproterozoic rocks of the Baoulé-Mossi domain are poorly exposed (Lompo, 2010; Metelka et al., 2011). The use of geophysical techniques to resolve shallow and deeper structures is essential for a better understanding of the structural configuration of the domain at depth.

The magnetotelluric (MT) method has proven itself highly useful in imaging the lithospheric structures and geometries of various Archean and Proterozoic domains. Major tectonic features are often revealed through compositional variation and deformation in rocks, as expressed through their electrical conductivity, and particularly the presence of

* Corresponding author.
E-mail address: flepape@cp.dias.ie (F. Le Pape).
[1] Now at: Complete MT Solutions, Inc., Canada.

http://dx.doi.org/10.1016/j.precamres.2017.08.013
Received 27 January 2017; Received in revised form 4 August 2017; Accepted 7 August 2017
Available online 08 August 2017
0301-9268/

conductive graphite, sulfides or saline fluids, whose resolved geometry can help understand the tectonic evolution of suture zones (e.g., Jones et al., 2001; Selway et al., 2009; Miensopust et al., 2011; Khoza et al., 2013). Although lithospheric-scale regional geophysical studies, and particularly MT, have not, to date, been routinely undertaken in West Africa, Ritz (1983, 1984) highlighted the extension of several major tectonic discontinuities deeper in the crust and lithosphere, based on the resistivity modeling of magnetotelluric profiles from northern Burkina Faso, southern Niger and Senegal. More recently Jessell et al. (2016) compiled the existing regional- and global-scale geophysical datasets to help provide a craton-scale framework for future studies.

In this study, we aim to provide further depth constraints on the main granite-greenstone assemblages of south-western Burkina Faso described by Baratoux et al. (2011) and Metelka et al. (2011). As part of the West African Exploration Initiative (WAXI) project, broadband and long period magnetotelluric data have been collected along a profile crossing the major lithological units of southern Burkina Faso. The MT data were modeled, using an objective inversion approach, to generate a three-dimensional (3D) resistivity model of the crust of southern Burkina Faso. A new density model was also obtained from forward modeling of ground gravity data acquired along the same transect as the MT data. In order to investigate the evolution at depth of the geophysical properties characterizing the different lithological units observed at the surface, the 3D resistivity model, as well as new gravity model, are discussed and compared with the gravity/geology forward model from Baratoux et al. (2011), and previously unpublished density and magnetization models of the area based on the joint inversion algorithm of Gallardo (2007).

2. Geological background

The Baoulé-Mossi domain formed in the Paleoproterozoic between 2250 and 1980 Ma and was subjected to several deformation phases associated with the Eburnean orogeny (Bonhomme, 1962; Feybesse et al., 2006; Baratoux et al., 2011). Further north and west, the Paleoproterozoic basement is overlain by the Mesoproterozoic to Paleozoic Taoudeni basin (Fig. 1) (Bronner et al., 1980; Teal and Kah, 2005; Rooney et al., 2010).

The greenstone belts of south-western Burkina Faso, extending into northern Ivory Coast and Ghana, show mafic tholeiitic compositions related to oceanic plateaus (Abouchami et al., 1990) and intermediate to felsic calc-alkaline compositions typical of volcanic arc environments (Béziat et al., 2000). The Birimian volcanic rocks characterizing the greenstone belts are overlain by flysch-type sedimentary basins (Baratoux et al., 2011). The Tarkwaian-type sediments, which were deposited after 2120 Ma, have been established as the youngest sequence in the greenstone belts of the Baoulé-Mossi domain (Leube et al., 1990; Bossière et al., 1996; Castaing et al., 2003; Feybesse et al., 2006; Baratoux et al., 2011). The peak of the Birimian volcanism has been dated around 2190–2160 Ma (Davis et al., 1994; Lüdtke et al., 1999; Loh and Hirdes, 1996) whereas Birimian sedimentary basins were dated as young as 2130 Ma (Lüdtke et al., 1999) and 2107 Ma (Doumbia et al., 1998). Therefore, whereas Leube et al. (1990) proposed the volcanic sequences and sedimentary basins to be contemporaneous, some of the sedimentary basins appear to postdate the principal volcanic activity (Agyei Duodu et al., 2009; Baratoux et al., 2011).

Western Burkina Faso is characterized by three N−S trending greenstone belts (Fig. 1), defined from west to east as the Banfora, Houndé and Boromo belts (Castaing et al., 2003). Each of them exhibits a similar stratigraphic sequence consisting of basalts and andesites at the base and evolving into volcano-sediments towards the top (Baratoux et al., 2011). The Banfora belt is separated into two parts by the Greenville-Ferkessedougou-Bobo-Dioulasso shear zone (GFBSZ) (Fig. 1) associated with synkinematic granitic intrusions (Lemoine, 1990). East of the GFBSZ, the Banfora belt is composed of basalts, andesites, volcano-sediments and rhyolites, whereas the west of the GFBSZ exhibits volcano-sedimentary sequences only (Baratoux et al., 2011). The Houndé belt shows intermediate to acid calc-alkaline volcanic series in its western part along the Ouango-Fitini shear zone (Fig. 1). To the east, the Boni shear zone characterizes the contact between tholeiitic basalts and gabbro, and Tarkwaian-type sediments. The Tarkwaian-type sedimentary unit represents a 400-km-long corridor stretching down into the Ivory Coast (Fig. 1) (Bossière et al., 1996). The eastern and western parts of the Boromo belt are characterized by a thick sequence of basalts intercalated with gabbros, including also more intermediate and ultramafic units in its eastern part. As it continues into Ghana, the Boromo belt becomes the Wa-Lawra belt (Leube et al., 1990; Duodu et al., 2009; Block et al., 2015). All rocks in this region have been metamorphosed to at least greenschist facies (Baratoux et al., 2011).

The granitoid domains separating the different greenstone belts have been named from west to east as the Niangoloko, Sidéradougou and Diébougou domains (Fig. 1). In addition to the well-defined granitoid domains, plutons have also intruded the greenstone belts as relatively small individual granite bodies (Baratoux et al., 2011; Metelka et al., 2011). There is evidence for only a few magmatic episodes contemporaneous with the Birimian volcanism since most of the plutonic activity occurred at a later stage through several magmatic pulses dating between 2180 and ~2097 Ma (Hirdes et al., 1996; Doumbia et al., 1998; Castaing et al., 2003; Duodu et al., 2009).

3. Magnetotelluric soundings

3.1. Data acquisition and processing

Magnetotelluric impedances, which contain information about the lateral and vertical variations in electrical conductivity of the subsurface, are obtained from recording the Earth's natural electromagnetic (EM) variations with time. In the frequency domain, the MT transfer function Z or MT impedance tensor describes the direct linear relationship between the measured horizontal components of the electric (E_x, E_y) and magnetic (H_x, H_y) fields (Chave and Jones, 2012).

As part of the West African Exploration Initiative (WAXI) project, MT data were collected in southern Burkina Faso between February and March 2013 using broadband (BBMT) Phoenix Geophysics (Toronto) MTU5A and long period (LMT) LEMI-417M (Lviv Centre of Institute for Space Research) instruments with an approximate 10 km spacing between BBMT sites, every 30 km for the LMT stations. The orientation of the profile was chosen to cross perpendicularly most of the north–south trending greenstone belts and granitoid domains of southern Burkina Faso (Fig. 1). The MTU5A recorded electric and magnetic time series data were processed using the standard robust processing of the commercial code from Phoenix Geophysics based on Jones and Jödicke (1984), which is based on a Least Trimmed Squares robust technique proposed independently by Rousseeuw (1984). When available, the LEMI-417 long period data (only acquired at sites bur013, bur020, bur023, bur026, bur028 and bur033) were processed following the method of Smirnov (2003). The BBMT data were recorded over 3 days whereas the LMT stations were left in the ground for around 20 days. Some of the broadband data are a noisier for periods above 100 s and some points had to be removed prior to inversion. Where possible the broadband and long period data were merged at common locations for periods between 100 and 1000 s, considering the broadband data as the shifting reference, i.e, if necessary the LMT apparent resistivity curves were shifted vertically to match the BBMT curves. Overall the data overlap well. Multiple sites were recorded simultaneously, enabling the use of remote referencing methods (Gamble et al., 1979) in order to reduce bias effects and improve the quality of the estimated MT responses. For this study, we limit the periods of investigation from 0.01 s to 1000 s, i.e., frequencies of 100 Hz to 0.001 Hz. As the main focus here is the investigation of the crust beneath southern Burkina Faso, it

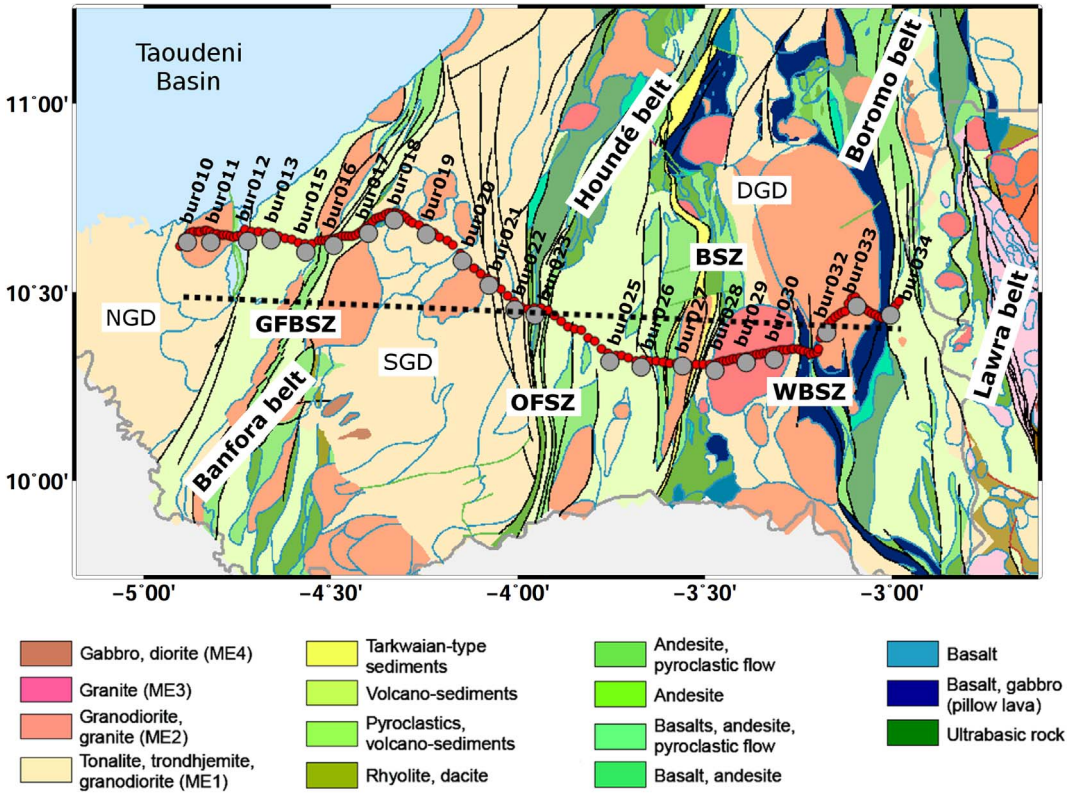

Fig. 1. Geological map of the study area (modified from Baratoux et al., 2011; Metelka et al., 2011; Block et al., 2015) showing major structural and geological features. The locations of the MT sites are represented as dark grey dots. The red dots represent the ground gravity measurement points. The black dotted line defines the location of the 2D density/magnetization geospectral image issued from joint inversion of gravity and aeromagnetic data. NGD = Niangoloko Granitoid Domain; GFBSZ = Greenville-Ferkessedougou-Bobo Dioulasso Shear Zone; SGD = Sidéradougou Granitoid Domain; OFSZ = Ouango-Fitini Shear Zone; BSZ = Boni Shear Zone; DGD = Diébougou Granitoid Domain; WBSZ = West Batié Shear Zone. (For interpretation of the references to color in this figure legend, the reader is referred to the web version of this article.)

was determined that periods ranging up to 1000 s penetrate sufficiently deep to resolve the whole crust due to the high resistivity of the area. Furthermore, it appeared the effects of the equatorial electrojet (Mareschal, 1986) were negligible for period below 1000 s but should be taken into account for more lithospheric scale studies including periods above 1000 s. No vertical magnetic component was recorded on the BBMT stations. For the LMT stations, induction vectors were considered but they are strongly affected by the equatorial electrojet. It is the case for even shorter periods than 1000 s compared to the effects of the electrojet on the impedance tensor mainly appearing for periods higher than 1000 s as mentioned above.

3.2. Data, phase tensor and dimensionality analysis

Data quality is generally good at most stations. Figs. 2a and 4 show the four components of a some selected sites across the profile. A lot of sites exhibit phases out-of-quadrant, which is a clear evidence of a 3D response due to local galvanic distortion or 3D subsurface resistivity. High apparent resistivity values can also be seen in all components for several stations highlighting the complexity of the study area and justifying the use of full tensor inversion. For instance, the responses of the MT tensor diagonal elements XX and YY cannot be neglected even when rotating the data in any particular strike direction. Moreover, due to the complexity of the tectonic setting, sites show different levels of distortion such as static shifts. For example, the significant split in the apparent resistivity curves at high frequency for site bur021 (Fig. 2a) may be associated with static shift. However, the static shift problem can be very tricky as at a single site not all curves may necessarily be affected and sometimes just one or two can be shifted up or down. It is worth mentioning also that sites bur024 and bur031 were not considered for this study since the responses were highly distorted, which explains the gaps observed in the MT profile (Fig. 1). As discussed below those stations were still included in the early stage of the modeling but discarded on the final results.

The MT phase tensor (Caldwell et al., 2004) represented as an ellipse is a useful tool to obtain qualitative information about the dimensionality and distribution of the regional conductivity structures in a 3D environment. In isotropic 2D cases, the ellipse axes are parallel and perpendicular to the 2D strike direction. However, in 3D cases, the coordinate-invariant skew angle β defines the deviation of the phase tensor principal axes from an equivalent symmetric configuration resulting from the asymmetry of the phase responses produced by 3D structures (Heise et al., 2006). Fig. 2b highlights the phase tensor skew values at each site for different periods (equivalent to depth) which also reveals the complexity of the data over the whole profile. It is however important to keep in mind that due to the non-representation of error of the ellipses plots, one must be careful when interpreting the phase tensor plots. The skew angles show a significant number of frequencies and sites with values outside the $[-5^\circ\ 5^\circ]$ interval and therefore exceeding the limits of 2D approximations. Overall, long periods exhibit relatively high skew values. However, for shorter periods, the ellipses define a mix between 2D and 3D-like clusters across the profile which appear to be consistent with lithological units (Fig. 1). The granitoid domains ellipses are defined by low β values and show consistent orientations between several neighbour sites. For sites located on or at close proximity to the greenstone belts, ellipses show high β values and more abrupt changes in orientations between neighbour sites. Furthermore, flattened ellipses observed at very short periods (< 0.1 s) for sites bur016 and bur023 can be explained by the presence of very high conductivity contrasts related to the major shear zones (Fig. 2b). The ellipses orientations show good agreement with the north–south trend of the greenstone belts and shear zones characteristic of the study area

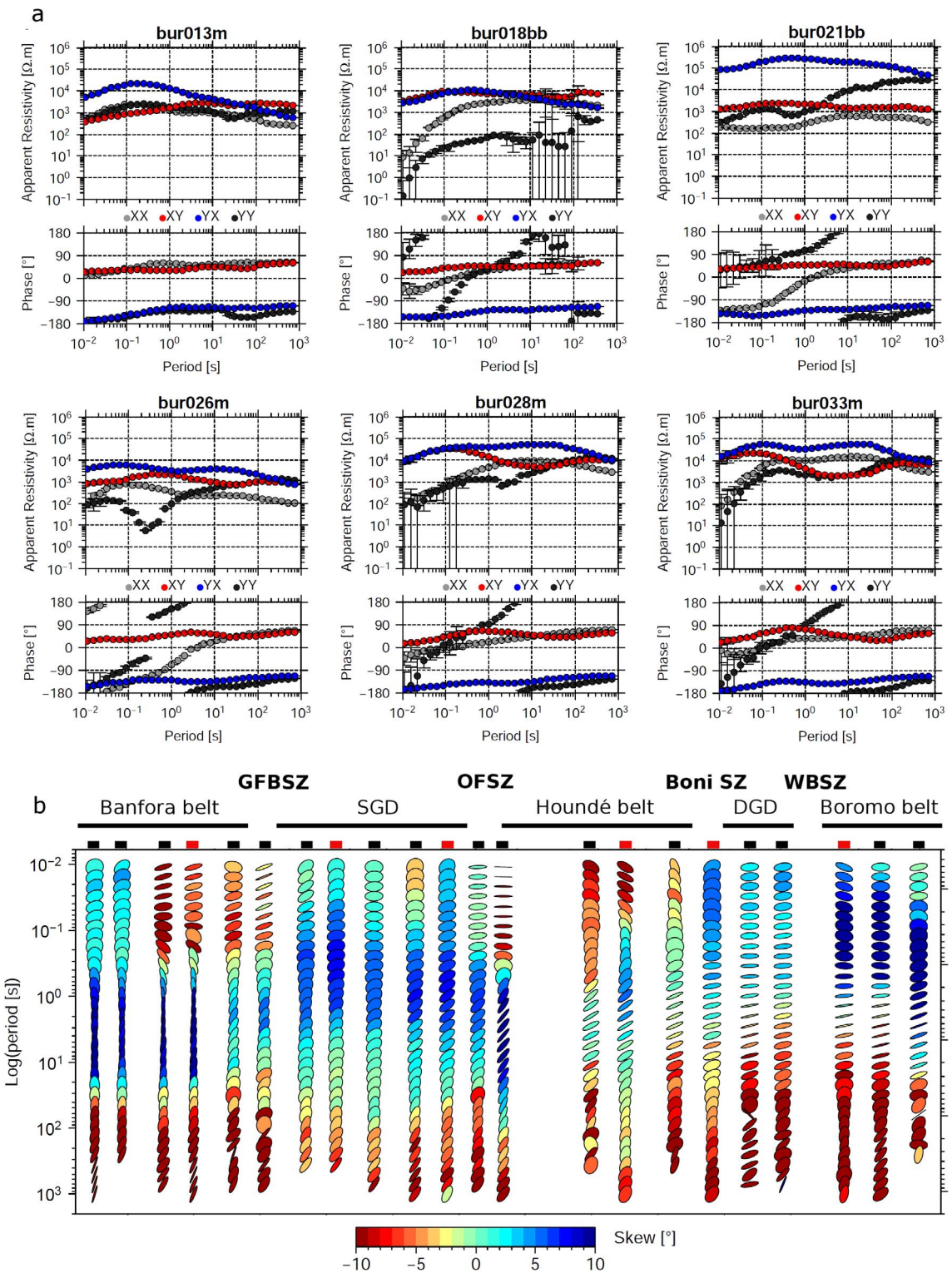

Fig. 2. a – MT full responses in apparent resistivity and phase for selected broadband (bb) and merged (m) sites along the profile. b – Phase tensor ellipses for all periods of each MT sites. The ellipses are normalized by their major axis and filled with the skew angle. The phase tensor ellipses are plotted so that the horizontal orientation corresponds to an east–west orientation.

(Figs. 1 and 2b). However, although the data show some 2D-like behaviour for clustered sites and periods, the 3D signature is too broad and significant to be neglected.

4. 3D resistivity modeling

Despite the "single-profile" layout of the stations, which is not optimal for 3D modeling/inversion, the significant 3D signatures of the responses for a broad range of MT stations requires the use of 3D approaches. Having only MT data collected along a single profile, 2D modeling of the data should be the default dimensionality, however the 2D modeling of 3D data brings significant artefacts in the final models inhibiting interpretations (Ledo, 2005).

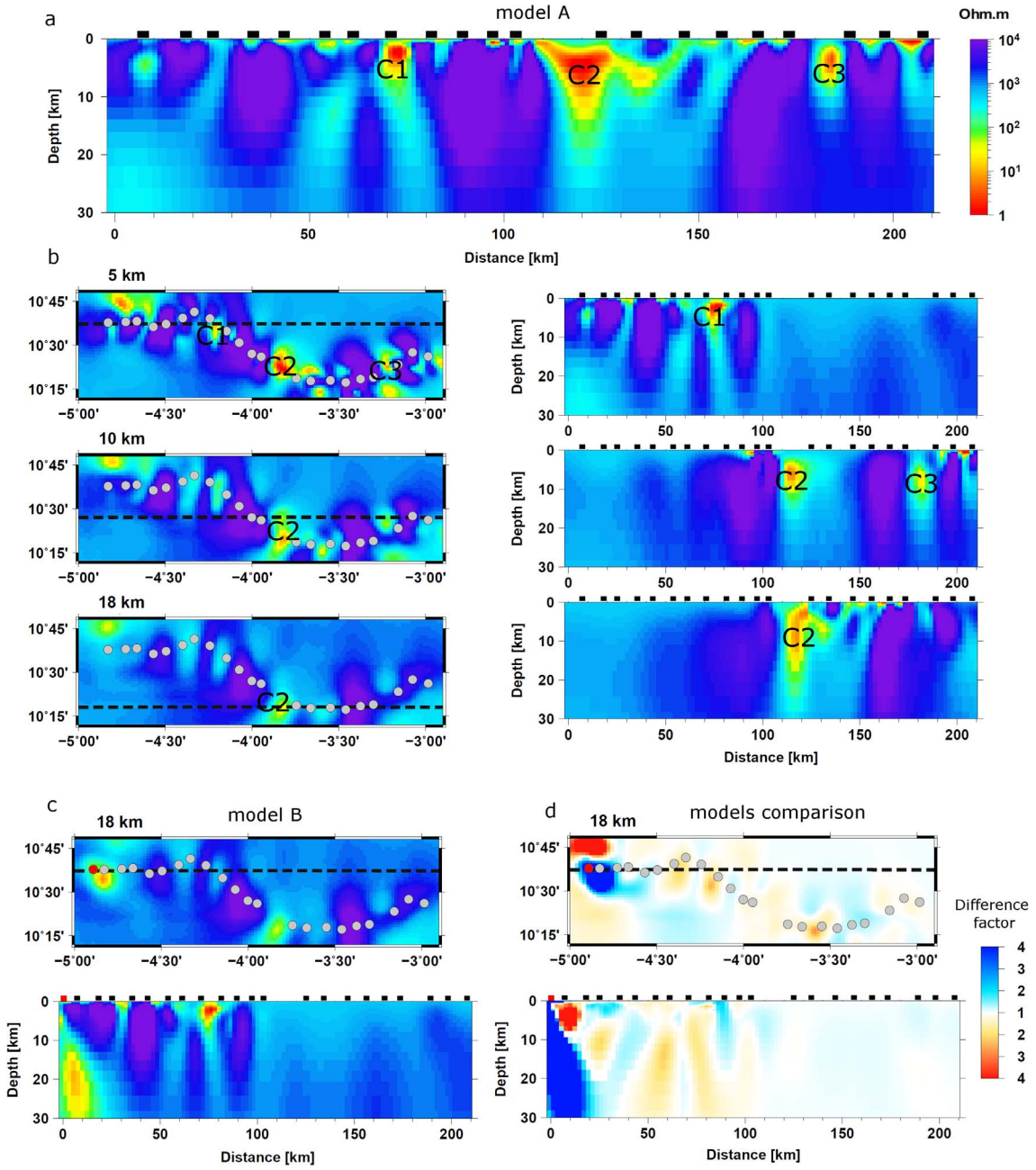

Fig. 3. a – 2D cross-section representative of 3D model A; b – 3D model A: Horizontal slices for different depths as well as vertical cross-sections (locations defined by black dashed lines); c – 3D model B: 18 km depth horizontal and a vertical cross-section (location defined by black dashed line) highlighting the presence of the lower crustal conductor below station bur010; d – Comparison of the resistivity ratio between model A and B: blue meaning A is more conductive than B and red meaning B is more conductive than A. (For interpretation of the references to color in this figure legend, the reader is referred to the web version of this article.)

4.1. 3D full tensor inversion

Two 3D inversion codes WSINV3DMT (Siripunvaraporn et al., 2005) and ModEM (Egbert and Kelbert, 2012) as well as different inversion steps were considered through the inversion process. At the end, mainly the code ModEM was used for models testing and to compute the final 3D models due to a faster convergence of the code to an acceptable misfit. However, it is worth noting that results from both inversion algorithms revealed similar structures, including conductors, which is also comforting the robustness of the inversion results presented here. The data were inverted simultaneously for all 4 impedance tensor elements and an error floor of 5% was used to set a minimum error bar of $0.05 * \mathrm{sqrt}(Z_{xx}Z_{yy})$ on the diagonal and $0.05 * \mathrm{sqrt}(Z_{xy}Z_{yx})$ on the off-diagonal elements of the impedance tensor during the inversion. Although different starting models have been tested, the starting (and a priori) model used for the initial inversion was a 150 km thick layer of 500 Ω m with resistivity decreasing gradually from 150 km to 410 km where a fixed 10 Ω m halfspace was locked during inversion. The later represents the mantle transition zone and is necessary in 2D and 3D modeling to prevent bleeding down of features and satisfy the boundary condition at the base of the model. The 3D mesh used for the inversions is defined as 81 × 152 × 51 cells with a 2 × 2 km horizontal gridding at the vicinity of the stations. Periods ranging from 0.01 s to 1000 s were modeled for crustal structures, which were assumed to extend to the average Moho depth of 30 km beneath the profile (Pasyanos and Nyblade, 2007). 3D inversions were performed in several steps where different schemes and station combinations have been tested. As mentioned previously, stations bur024 and bur031 were not considered in

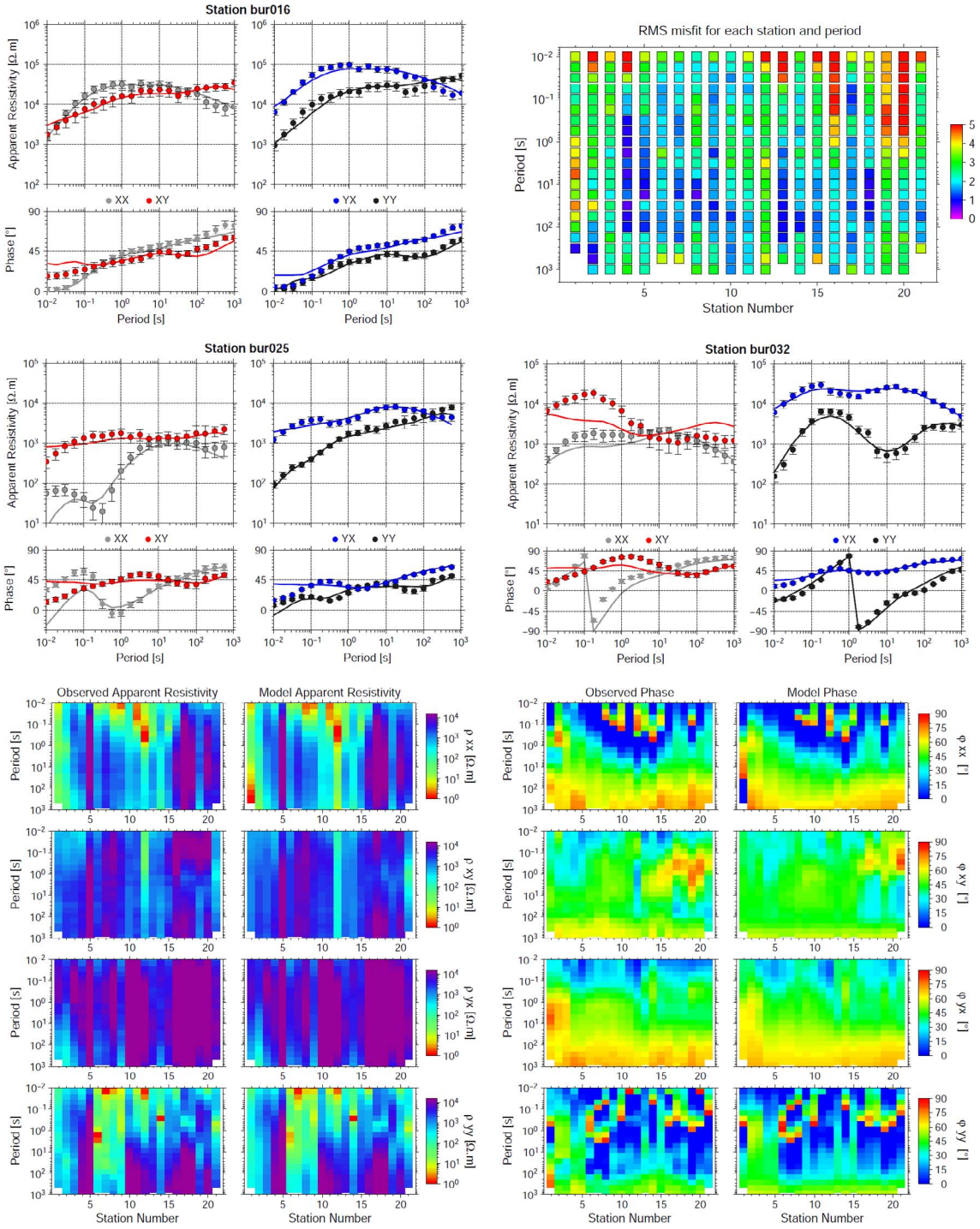

Fig. 4. Observed and predicted apparent resistivity and phase responses for 3D model A. The fit between the observed (dots) and modeled (lines) 4 components curves for 3 particular sites is shown as well as the normalized misfit between observed and calculated data for each station and each period. At the bottom, all responses are plotted for all 4 components of the impedance tensor as a function of period and station location along the MT profile. Station numbers are increasing from west to east.

the final results due to some highly distorted responses characterized by higher misfits in the inversions. Removing those stations however did not significantly affect the structures of the models, for example by adding or removing conductive anomalies. Furthermore, two particular schemes were investigated in the inversion steps. Inversions have been performed (1) by modeling higher frequency first and introducing progressively the lower frequencies but also (2) by modeling longer periods first and introducing progressively the higher frequencies. Both schemes led to similar structures. For this data set, inverting the high frequencies first introduced shallow structures “locked” through the different iterations and therefore affecting the data fit for some stations at longer periods. However, inverting for long period first helped improve the fitting of the long period data as well as the higher frequency data associated with shallower structures. Finally, the effects of some sites have been tested, but as discussed below the main differences were observed for the least constrained sites located at the extremities of the profile.

4.2. Model A vs model B

The two best models obtained from ModEM and highlighting consistent structures through the different inversion tests, including conductors C1, C2 and C3, are discussed in Fig. 3. Whereas model B was obtained after inverting all 22 sites (Fig. 3c), the preferred model A (Fig. 3b) did not include site bur010 in the inversion. Both models are very similar but, as shown by Fig. 3d, they differ in the location of the conductive anomaly observed on the western end of the profile (below station bur010). Whereas model B places the anomaly in the middle and lower crust beneath the profile, model A places the anomaly north of the profile in the upper crust. This anomaly is likely real as it is seen by more than one station, however being located at the edge of the profile, its location becomes poorly constrained by the lack of data coverage. The comparison of models A and B shows that interpretation of 3D inversion of a single profile must be taken with care. The lack of constraints on anomalies derived from 3D inversions of single profiles have been discussed in Kiyan et al. (2013) and Wei et al. (2014). Despite being seen by the data, the locations of certain anomalies are not well constrained particularly at the edges of the profile. Further tests have also been carried out by removing other stations to determine their influence on the final models, but most observed features remained quite robust. Furthermore, whereas model A shows an overall normalized Root Mean Square (nRMS) misfit of 2.7, model B is defined by an nRMS of 2.95. The difference in nRMS between model A and B is mainly reflecting a better fit of the data (not only for western sites) due to the absence of a lower crustal conductor right below the profile brought by station bur010. Therefore model A was chosen as the preferred model for the area. Despite being associated with a better fit to the overall data, the conductive anomaly observed on model A off-profile (north-west of horizontal slices Fig. 3b) is still not well constrained and will not be discussed further in this paper.

4.3. Final 3D resistivity model A

The observed and predicted apparent resistivities and phases from model A are compared on Fig. 4 for all 4 components of the tensor. Overall, the observed and modeled data are very similar, showing only some localized exceptions. The comparison of observed and predicted curves show that the 3D characteristic of the data, such as phases out-of-quadrant as well as XX and YY component, are relatively well fitted. For example, the observed and predicted responses for site bur025, close to conductor C2, reveal higher misfits at high frequencies but overall the data are quite well recovered. Despite having some of the worst misfits localized at shorter periods for a few stations, Fig. 4 shows that the data fit between observed and modeled responses remains quite good at shorter periods for all four components of the tensor. This observation can be mainly accounted for the use of a fine grid (2×2 km) in close proximity to the stations which significantly improved the resolution on 3D effects for shorted periods and particularly for XX and YY components. The use of a finer mesh would eventually improve the modeling of shorter periods but grid size was limited by computation resources.

The 2D cross-section derived from the 3D model A and presented on Fig. 3a defines a good representation of the most robust resistive and conductive features characterizing the crust of southern Burkina Faso. Generally, the main features in the data that can be seen on the responses (Figs. 2 and 4) are quite well represented in the resistivity model (Figs. 3a and 3b). The 3D model particularly highlights the juxtaposition between highly resistive (purple) and less resistive (green) areas corresponding to the surficial signature of the granitoid domains as well as granite intrusions and greenstone belts, respectively. Overall, the crust beneath southern Burkina Faso is quite resistive with major lateral changes correlating very well with the observed geology (Fig. 3). It is worth noting that compared to the greenstone belts, the lower crust of the granitoid domains is very resistive which may highlight a difference in composition of the lower crust or difference in past alteration. The Greenville-Ferkessedougou-Bobo Dioulasso Shear Zone (GFBSZ), Ouango-Fitini Shear Zone (OFSZ) and Boni Shear Zone (Boni SZ) are defined by large resistive contrasts that extend to the lower crust. On the other hand, the West Batié Shear Zone (WBSZ) which divides two highly resistive blocks of the Diébougou Granitoid Domain (DGD) does not seem to extend further than the middle crust. The Sidéradougou Granitoid Domain (SGD) is divided into two parts: a highly resistive eastern bloc extending probably further into the mantle and a western part more heterogeneous, alternating resistive and more conductive features, which might be linked to the GFBSZ at depth. Finally, three significant conductive anomalies located in the upper crust can be observed on the resistivity model. From west to east, they are defined as conductors C1, C2 and C3 (Figs. 3a and 3b). Conductive anomaly C1 is very localized and is found in the first 5 km of the SGD crust. The anomaly C2 is the most significant in terms of depth and width and is associated with the Houndé belt. Finally, conductive anomaly C3 is located right on the WBSZ.

5. Gravity data and modeling

Ground gravity data were acquired along the same profile as the MT data, with an average spacing of 2 km between each recording point. The ground gravity data were measured using a gravimeter Scintrex CG-3. This device registered 120 measurements at each location and an average value was provided. Data processing includes tide correction, instrumental drift correction (some points were measured multiple times) and latitude correction (calculated using 1967′s formula of Sheriff, 1984). A differential Ashtech GPS system was used for accurate positioning. The Bouguer anomaly was derived using a density value of $2.67 g/cm^3$ taking into account SRTM topography within a radius of 40 km around each recording site. A low-pass filter corresponding to wavelengths above 10 km was applied on the Bouguer anomaly in order to focus the modeling on large-scale density contrasts for better comparison with the resistivity model. It is also worth noting that the regional Bouguer anomaly associated with a low-pass filter above 200 km revealed an overall anomaly decreasing from west to east, which could reflect variations of density at depth and particularly lateral changes in the Moho. However, according to Pasyanos and Nyblade (2007) if any change in the Moho occurs at depth beneath the profile, it would likely correspond to a reduction of the crustal thickness towards the eastern end of the profile, which would generate an opposite trend in the evolution of the gravity anomaly along the profile (low to high anomaly from west to east). As a consequence, the regional Bouguer anomaly for wavelengths above 200 km was kept for modeling of the data, assuming the overall variations were more likely related to shallower structures. Observed gravity anomalies can be explained by a variety of mass distributions at different depths. The forward modeling of the gravity data was performed using the gravity tool implemented within the WinGLink package of formerly Geosystem, now Schlumberger. The density model (Fig. 5b) was obtained from forward modeling of the Bouguer anomaly data (Fig. 5a) taking into account the resistivity contrasts observed on the 3D resistivity model as well as surficial geology and gravity models from Baratoux et al. (2011).

For consistency with the density values described in Metelka et al. (2011) and Baratoux et al. (2011), similar densities were considered for the different sequences. However, since a low-pass filter was applied on the Bouguer anomaly, the modeled density values represent more of an average density, or deviations from a reference value, rather than absolute density values. A reference density of $2.75 g/cm^3$ was chosen for most of the crust based on density values for granitoid domains (Baratoux et al., 2011). Granitic intrusions were assumed a density of $2.7 g/cm^3$, except for the pluton intrusions at the proximity of the Boromo belt for which densities were assumed as low as $2.65 g/cm^3$. The greenstone belts were modeled with densities of 2.8, 2.85 and $2.9 g/cm^3$ reflecting differences in the volcanic lithologies observed at

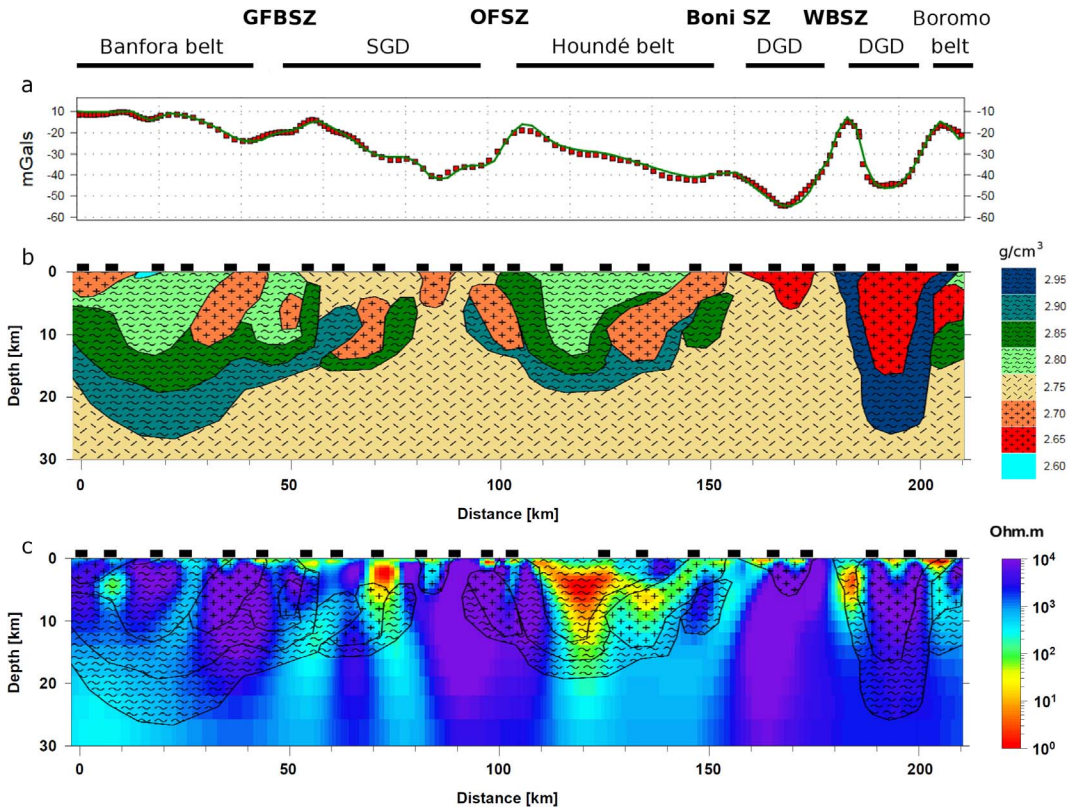

Fig. 5. a – Gravity Bouguer anomaly; b – Density model derived from forward modeling of the ground gravity data; c – Comparison of the gravity model with the resistivity structures obtained from MT modeling.

the surface. A density of 2.95 g/cm^3 for the more mafic to ultramafic rocks exposed west of the Boromo belt corresponds to significant gravity highs. Although less extensive around the recording area, the eastern part of the Banfora belt, in the vicinity of the GFBSZ, is characterized by the presence of more widespread basalts and andesites further south of the profile. Since they are not apparent at the surface along the profile, those units were modeled at depth with higher density values in order to explain the observed gravity high. Similarly, the mafic rocks associated with the OFSZ were also modeled with higher densities (Fig. 5b). Furthermore, it is worth noting that the Banfora greenstone belt appears to be thicker than the Houndé belt, assuming both belts have more or less the same composition, i.e., the same densities of the same lithologies. In order to obtain relatively similar thickness of high density material for the Houndé belt, the volume or size of less dense granitic material would have to be increased.

Resistivity and density do not have a straightforward relationship but they can still be compared qualitatively. In this study, greenstone belts associated with denser material appear as more conductive features, particularly the Houndé belt, and the granitoid domains related to less dense material reflect very high resistivities (Fig. 5c). Such relationships bring some further constraints on the evolution of the different tectonic features with depth. Conductivity gradients revealed by the phase tensor data (Fig. 2) can also be correlated with the steeper gravity gradients from the Bouguer anomaly data (Fig. 5a) observed close to the main shear zones. There are several density features that correlate fairly well with the resistivity cross-section (Fig. 5c). One feature that particularly seems to be very well constrained by the resistivity model is the large granitic body (Gaoua batholith) located east of the WBSZ between mafic lithologies. Furthermore, the less dense volcanic lithologies of the Houndé belt correlate very nicely in depth and width with the highly conductive anomaly C2 (Fig. 3). Finally, the fact that based on the gravity model the Banfora greenstone belt is extending further in depth west of the GFBSZ, helps explaining the differences in resistivity between the western and eastern part of the SGD. It is important to keep in mind that a more complex gravity model, with sharp contrasts as seen in the resistivity model, could probably fit the Bouguer anomaly as well. However, the aim here was to present a relatively simple “geological” density model that match with the surficial geology and help understand better the observed resistivity contrasts at depth.

6. Discussion

6.1. Electrical resistivity of southern Burkina Faso

Overall, apart from the top 3 km, the main shear zones and conductive anomalies C1, C2 and C3 localized in the upper crust, most of the crust is remarkably resistive throughout its whole extent. Although differences in resistivity are fairly clear between greenstones belts and granitoid domains, there is no significantly conducting lower crust, which is usually observed in continental settings (Jones, 1992; Hyndman et al., 1993). Furthermore, conductive lower crust has also been imaged in stable plate interiors, although less expected when compared to Paleozoic regions. Parts of the Kaapvaal and Zimbabwe cratons in south Africa (Muller et al., 2009; Miensopust et al., 2011; Khoza et al., 2013) but also the northeastern Rae craton region in Canada where Evans et al. (2005) revealed the presence of a broadly conductive lower crust (50 Ω m). The enhanced conductivity of the lower crust pervasively observed in Proterozoic and younger terranes has been explained by the presence of saline fluids (Jones, 1987, 1992; Hyndman et al., 1993; Wannamaker, 2000), although they may not be stable at those depth (Yardley and Valley, 1997). Graphite films along grain boundaries have also been proposed to be good candidates (Hyndman et al., 1993), although mechanical deformation could affect graphite connectivity in the lower crust (Glover, 1996) and recent laboratory experiments would appear to exclude this hypothesis (Yoshino

and Noritake, 2011). The highly resistive lower crust of southern Burkina Faso is more likely defined by the presence of dry granulite rocks characterized by a lack of extensive interconnected graphite films. Spratt et al. (2009) also imaged a resistive lower crust beneath the Proterozoic Wopmay orogen abutting the Slave Craton. Finally, it is worth noting that Ritz (1983) also highlighted the presence of a resistive lower crust in northern Burkina Faso, consistent with our results.

The upper crust however shows larger conductivity contrasts and reveals the presence of three striking conductive anomalies (< 50 Ω m). The relatively low resistivity of the greenstone belts, and particularly the Houndé belt, can be explained by the presence of the volcano-sediments in the upper crust but also by the broad number of faults, in contrast to the granitoid domains (Fig. 1). The faults and shear zones present within or at the boundary of the greenstone belts create pathways for fluids, increasing the overall bulk conductivity. Those fluids could also have precipitated into more conductive phases such as graphite or sulfides. Kříbek et al. (2008) discussed on the presence of graphite in sub-greenschist and greenschist facies of the Kaya-Goren greenstone belt, an extension of the Houndé belt in northern Burkina Faso. In the case of the Houndé belt, the conductivity anomaly C2 matches very well with the volcano-sediments belonging to the Lower Birimian sequence (Feybess and Milesi, 1994; Kříbek et al., 2008) and could therefore be as well explained by the presence of graphite in the sequence. To the east, the conductive anomaly C3 characterizing the WBSZ is also significant. It is worth mentioning the presence further north of the Perkoa massive volcanogenic sulfide deposit hosted by the Lower Birimian sequences of the Boromo Belt (Schwartz and Melcher, 2003). Therefore, other sulfide-rich intrusion may have happened further south on the western flanks of the Boromo belt. The anomaly however could also be linked to the presence of fluids or crystallized graphite along the shear zone. Finally, the last significant conductive anomaly C1 observed on the profile and located in the middle of the Sidéradougou domain does not seem to match with any particular fault or shear zones, the Bossié shear zone (Baratoux et al., 2011) being located more to the east. However, it correlates quite well with a high magnetic contrast which is discussed below.

6.2. Crustal structure interpretation

The cross-gradient inversion scheme of Gallardo (2007) has been applied to gravity (NGA/BGI) and magnetic (BUMIGEB aeromagnetic survey derived grids) datasets for Burkina Faso. The cross-gradient inversion technique mainly focuses on the structural similarity between the distribution of different geophysical properties, reducing the non-uniqueness of the inversion process for each data type. While the density and magnetization models across southern Burkina Faso derived from cross-gradient inversion can be used for a correlative interpretation, we prefer to use the associated red-green geospectral image representation, as used in Gallardo and Thebaud (2012) and Gessner et al. (2016). This image bears the integrated structure-multi-property value representation and is presented in Fig. 6 in comparison with the new (inverse) resistivity and (forward) gravity models, as well as the gravity-geology forward model from Baratoux et al. (2011) matching in location with the eastern part of the MT profile. The density variations observed in Fig. 6d from Gallardo's inversion are in reasonably good agreement with the gravity models presented in Figs. 6a and 6b from forward modeling, exhibiting low and high density values for granitoid domains and greenstone belts, respectively. The resemblance to the MT section is more outstanding, showing high correlation of the most electrical conductors (labelled A to E on Figs. 6c and 6d) to deeper high magnetization/intermediate density features. It also shows a match of the major resistors to shallower greenstone and intrusive terrains identifiable in the geospectral image (e.g. feature labelled 1 on Figs. 6c and 6d). The variations of magnetization along the profile highlight relatively high magnetic contrasts at depth beneath the more mafic sequences associated with each greenstone belt. Variations in rock bulk susceptibility reflect mainly variations in magnetite content (Metelka et al., 2011). Compared to gravity, magnetic anomalies are more difficult to interpret since high magnetic mineral phases occur equally in granites and mafic rocks. However, it is worth noting that, in Burkina Faso, basalts and gabbros have been associated with high susceptibility anomalies and volcanic sediments with low anomalies, whereas granitoids reflect both low and high magnetization (Metelka et al., 2011). The Niangoloko granitoid domain (Fig. 1) does not seem to show a significant signature, either on the resistivity or the gravity models (Fig. 6), and it is undistinguishable from the Banfora belt signature in the geospectral image. According to all these evidences, it seems reasonable to expect that the Banfora belt may also expand further west at depth compared to its surficial trace (Fig. 7). Furthermore, one main difference between the Banfora belt and both the Houndé and Boromo belts is the observed broad lower magnetic signature of its upper crust (reflected in distinctive green tones in the geospectral image in Fig. 6d) compared to the other two belts showing high magnetic anomalies. This low magnetic anomaly of the Banfora belt is also presented in Metelka et al., 2011, indentifying the GFBSZ as a "set of demagnetized" shear zones. On the contrary, both Houndé and Boromo belts reveal highly magnetic mafic and ultramafic intrusions on their flanks that can account for the observed anomalies.

For the Sidéradougou and Diébougou granitoid domains, the low density structure observed in the geospectral image of Fig. 6d shows a clear correlation with the high resistivity of the crust extending across the whole crust. The Houndé belt shows a smaller density imprint than the Banfora belt. Assuming both belts can be modeled by similar density values, the Houndé belt cannot be modeled as thick as the Banfora belt unless intruded by more (low density) plutonic material. In fact, the density variations in Fig. 6d illustrate the presence of low densities in the eastern part of the Houndé belt. The OFSZ located west of the Houndé belt is associated with very high density and high magnetic heterogeneities (Figs. 6b and 6d) extending in depth and confirming the observations from the resistivity model that the OFSZ is a significant crustal feature that may be extending further in the mantle. Furthermore, in addition to other shear zones across the profile, the Boni shear zone bounding the east side of the Houndé belt also shows a strong contrast at depth in resistivity. The western part of the Boromo belt delimited by the WBSZ is clearly highlighted by all geophysical techniques, showing significant increases in density, resistivity and susceptibility. However, the geospectral image does not reveal the presence of the Gaoua batholith or the Boni shear zone located west of the Boromo belt, although its signature is quite clear on the new gravity and resistivity models (Fig. 5). This difference is explained by the absence of actual ground gravity data in the regional polygons used for joint inversion for this region. This also prevents the detection of any density-magnetization heterogeneity that may correlate to the marked conductor C3. Concerning the conductive anomalies C1 and C2, the magnetic and density signatures allow us to confirm or improve their interpretation. C1 and C2 have low density but correlate very well with a high magnetic blob, which corroborates with the interpretation of the presence of graphite. Although, as discussed above, C3 might not be properly resolved on the geospectral image (Fig. 6d), the observed lower magnetization associated with the conductive anomaly may be only related to the presence of fluids in the shear zone, instead of highly magnetic graphite or sulfides.

6.3. Structural constraints at depth

The geophysical models discussed here show clear correlations between each other and particularly bring further constraints at depth on the tectonic structures involved in the area. Overall, the major resistivity contrasts reveal the extension of major shear zones that divide or bound the main greenstone belts. The dipping orientations of the major contacts and shear zones have been plotted in Fig. 7. West of the

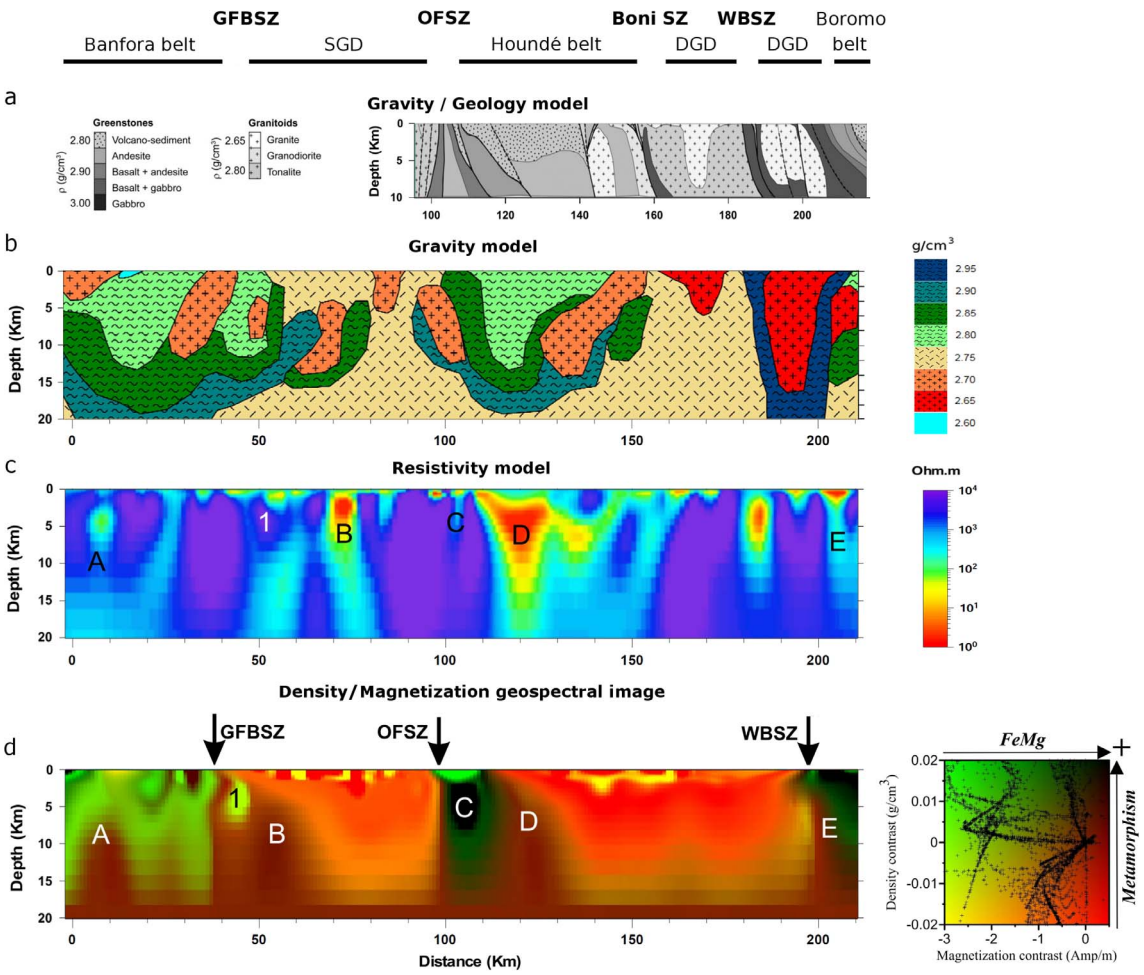

Fig. 6. Comparison of different geophysical models for the crust of southern Burkina Faso. a – Gravity/geology forward model from Baratoux et al. (2011); b – Preferred density model derived from forward modeling of ground gravity data; c – Resistivity model derived from MT 3D inversion; d – Density and magnetic geospectral representation issued from the joint inversion of gravity and magnetic data. The associated colors represent the relationship between density and magnetization contrasts.

profile, the GFBSZ is defined by west- and east-dipping structures. The geometry of the OFSZ system is in very good agreement with the gravity model from Baratoux et al. (2011) (Fig. 6a) showing two trends: a sub-vertical orientation to the west and a very pronounced eastward dipping structure to the east. Further east, although Baratoux et al. (2011) described the Boni shear zone as an east-dipping structure, the resistivity model reveals that the Boni shear zone might be dipping to the west instead. Moving closer to the Gaoua batholith, the structures, including the WBSZ, appear more sub-vertical. Those trends in the crustal scale resistivity contrasts are also seen and confirmed on the different vertical cross-sections of the 3D resistivity model (Fig. 3b). Furthermore, despite being a single profile, the horizontal slices through the 3D model at different depths (Figs. 3b and 7) highlight the preferred north–south orientated extent of the major shear zones as deep as the Moho. In fact, the lateral variations observed on the global Bouguer anomaly map compare quite well with the lateral distribution of the resistivity contrasts at depth, as well as the surficial geology (Fig. 7). Therefore, although the lateral resistivity variations at depth are associated with the modeling of a single profile, they still reveal some consistent and interesting information on the distribution of the main terranes deeper in the crust. The presence of sub-vertical and steeply dipping lateral resistivity contrasts, associated with major thrust faults and shear zones, that divide the whole crust and possibly extend into the mantle (Fig. 7), reflects the very strong shortening that affected the region through time. The observed large-scale signatures of the Greenville-Ferkessedougou-Bobo Dioulasso, Ouango-Fitini Shear Zone, Boni and West Batié shear zones may favour the model of crustal thickening through nappe stacking along parallel thrust faults (Hirdes et al., 1996; Feybesse et al., 2006; Baratoux et al., 2011).

7. Conclusion

As expected and clearly highlighted by the MT data, the Leo-man shield is a very difficult area to model and interpret. In such a complex tectonic setting, the modeling and interpretation of MT data can be quite challenging and the need for the integration of several geophysical techniques and data sets becomes significant. For instance, not only the multi- geophysical approach including density and magnetization contrasts defines a more robust interpretation of the main crustal features but it also comforts on the validity of the main features revealed by the 3D resistivity model. Overall, the results enable to differentiate and highlight the structure of the granite-greenstone formations of the Baoulé-Mossi domain at depth, but also reveal the extent of significant shear zones likely extending further in the mantle.

Acknowledgments

A big thank you to the SOS Sahel crew for their tremendous contribution in the planning and execution of the MT fieldwork but also for facilitating the communication with local villages. Special thanks the IRD centre in Ouagadougou and particularly Moumouni Koné and Frédéric Cazenave for their help and support during MT fieldwork preparation. We also would like to thank Sylvain Bonvalot for helping out with the gravimeter and Saga Sawadogo from the University of

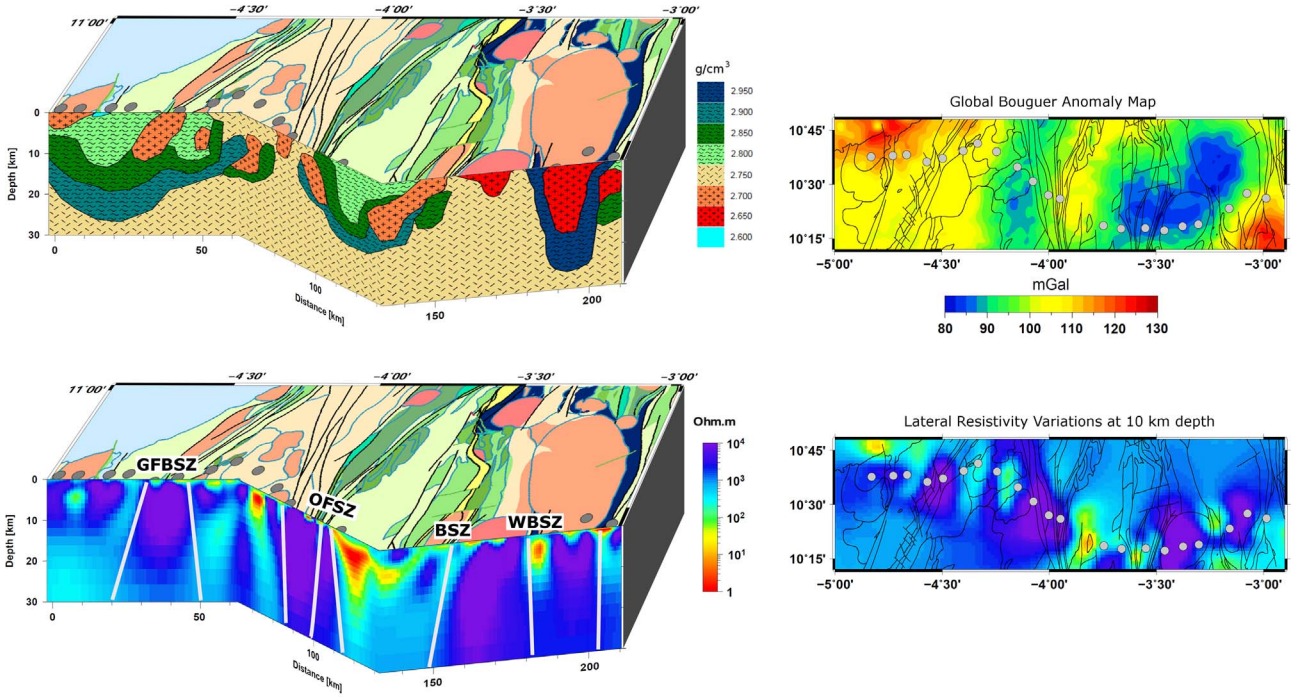

Fig. 7. Correlation between the density and resistivity contrasts of the crust at depth with surficial lithologies of southern Burkina Faso. The crustal scale resistivity contrasts interpreted as involved with major shear zones are highlighted in light grey. GFBSZ = Greenville-Ferkessedougou-Bobo Dioulasso Shear Zone; OFSZ = Ouango-Fitini Shear Zone; BSZ = Boni Shear Zone; WBSZ = West Batié Shear Zone. Lateral variations of the electrical resistivity at 10 km are also compared with the Bouguer anomaly map derived from the global 2 min resolution WGM2012 model (Balmino et al., 2012).

Ouagadougou for the logistics on the gravity fieldwork. This work was funded by the West African Exploration Initiative (WAXI), and we wish to gratefully acknowledge AMIRA International and the industry sponsors. Thank you also to Maxim Smirnov for providing his processing code, Weerachai Siripunvaraporn for providing the 3D inversion code WSINV3DMT and Gary Egbert for providing the 3D inversion code ModEM. We would like to thank the Irish Centre for High Performance Computing (ICHEC) for availing the FIONN cluster to carry out the numerical computations and Jan Vozar, Hao Dong and Gaofeng Ye for providing matlab visualisation tools for 3D MT results. Finally, special thanks to the local villagers for their help and welcoming during the installations of the magnetotelluric stations.

References

Abouchami, W., Boher, M., Michard, A., Albarède, F., 1990. A major 2.1 Ga event of mafic magmatism in West Africa; an early stage of crustal accretion. J. Geophys. Res., B, Solid Earth Planets 95 (17), 605–617 (629).

Agyei Duodu, J., Loh, G.K., Hirdes, W., Boamah, K.O., Baba, M., Anokwa, Y.M., Asare, C., Brakohiapa, E., Mensah, R.B., Okla, R., Toloczyki, M., Davis, D.W., Glück, S., 2009. Geological Map of Ghana 1:1,000,000. BGS/GGS, Accra, Ghana/Hannover, Germany.

Balmino, G., Vales, N., Bonvalot, S., Briais, A., 2012. Spherical harmonic modelling to ultra-high degree of Bouguer and isostatic anomalies. J. Geodesy 86, 499–520.

Baratoux, L., Metelka, V., Naba, S., Jessell, M.W., Gregoire, M., Ganne, J., 2011. Juvenile paleoproterozoic crust evolution during the eburnean orogeny (2.22.0 ga), western Burkina Faso. Precambr. Res. 191, 18–45.

Bessoles, B., 1977. Géologie de l'Afrique. Le craton Ouest-Africain mémoires. BRGM, Paris, pp. 88.

Béziat, D., Bourges, F., Debat, P., Lompo, M., Martin, F., Tollon, F., 2000. A Paleoproterozoic ultramafic-mafic assemblage and associated volcanic rocks of the Boromo greenstone belt: fractionates originating from island-arc volcanic activity in the West African craton. Precambr. Res. 101, 25–47.

Block, S., Ganne, J., Baratoux, L., Zeh, A., Parra-Avila, A.L., Jessell, M., Ailleres, L., Siebenaller, L., 2015. Petrological and geochronological constraints on lower crust exhumation during Paleoproterozoic (Eburnean) orogeny, NW Ghana, West African craton. J. Metamorph. Geol. 33, 463–494.

Bonhomme, M., 1962. Contribution à l'étude géochronologique de la plate-forme de l'Ouest Africain. Annals de la Faculté des Sciences de Université de Clermont-Ferrand Géol. Minéral 5 (62).

Bossière, G., Bonkoungou, I., Peucat, J.-J., Pupin, J.-P., 1996. Origin and age of Paleoproterozoic conglomerates and sandstones of the Tarkwaian Group in Burkina Faso, West Africa. Precambr. Res. 80, 153–172.

Bronner, G., Roussel, J., Trompette, R., 1980. Genesis and geodynamic evolution of the Taoudeni cratonic basin (Upper Precambrian and Paleozoic), Western Africa. Dyn. Plate Int. Geodyn. Series 1, 8190.

Caldwell, T.G., Bibby, H.M., Brown, C., 2004. The magnetotelluric phase tensor. Geophys. J. Int. 158, 457–469.

Castaing, C., Billa, M., Milési, J. P., Thiéblemont, D., Métour, J. L., Egal, E., Donzeau, M., Guerrot, C., Cocherie, A., Chèvremont, P., Tegyey, M., Itard, Y., Zida, B., Ouedraogo, I., Koté, S., Kabore, B. E., Ouedraogo, C., Ki, J.C., Zunino, C., 2003. Notice explicative de la carte géologique et minière du Burkina Faso à 1/1 000 000, 147.

Chave, A.D., Jones, A.G., 2012. The Magnetotelluric Method: Theory and Practice. Cambridge University Press, New York.

Davis, D.W., Hirdes, W., Schaltegger, U., Nunoo, E.A., 1994. U-Pb age constraints on deposition and provenance of Birimian and gold-bearing Tarkwaian sediments in Ghana, West Africa. Precambr. Res. 67, 89–107.

Doumbia, S., Pouclet, A., Kouamelan, A., Peucat, J.J., Vidal, M., Delor, C., 1998. Petrogenesis of juvenile-type Birimian (Paleoproterozoic) granitoids in Central Cote-d'Ivoire, West Africa: geochemistry and geochronology. Precambr. Res. 87, 3363.

Duodu, J.A., Loh, G.K., Hirdes, W., Boamah, K.O., Baba, M., Anokwa, Y.M., Asare, C., Brakohiapa, E., Mensah, R.B., Okla, R., Toloczyki, M., Davis, D.W., Glück, S., 2009. Geological Map of Ghana 1:1 000 000. BGS, GGS, Accra (Ghana), Hannover (Germany).

Egbert, G., Kelbert, A., 2012. Computational recipes for electromagnetic inverse problems. Geophys. J. Int. 189, 251–267.

Evans, S., Jones, A.G., Spratt, J., Katsube, J., 2005. Central Baffin electromagnetic experiment (CBEX) maps the NACP in the Canadian arctic. Phys. Earth Planet. Inter. 150, 107–122.

Feybesse, J.L., Milesi, J.P., 1994. The Archaean/Proterozoic contact zone in West Africa: a mountain belt of decollement thrusting and folding on a continental margin related to 2.1 Ga convergence of Archaean cratons? Precambr. Res. 69, 199–227.

Feybesse, J.L., Billa, M., Guerrot, C., Duguey, E., Lescuyer, J.-L., Milési, J.-P., Bouchot, V., 2006. The Paleoproterozoic Ghanaian province: geodynamic model and ore controls, including regional stress modeling. Precambrian Res. 149, 149–196.

Gallardo, L.A., 2007. Multiple cross-gradient joint inversion for geospectral imaging. Geophys. Res. Lett. 34 (L19301).

Gallardo, L.A., Thebaud, N., 2012. New insights into Archean granite greenstone architecture through joint gravity and magnetic inversion. Geology 40 (3), 215–218.

Gamble, T.D., Goubau, W.M., Clarke, J., 1979. Magnetotellurics with a remote magnetic reference. Geophysics 44 (1), 53–68.

Gessner, K., Gallardo, L.A., Wedin, F., Sener, K., 2016. Crustal structure of the northern Menderes Massif, western Turkey, imaged by joint gravity and magnetic inversion. Int. J. Earth Sci. (Geol Rundsch) 105, 2133.

Glover, P.W.J., 1996. Graphite and Electrical Conductivity in the Lower Continental Crust: a review. Phys. Chem. Earth 21 (4), 279–287.

Heise, W., Caldwell, T.G., Bibby, H.M., Brown, C., 2006. Anisotropy and phase splits in magnetotellurics. Phys. Earth Planet. Inter. 158, 107–121.

Hirdes, W., Davis, D.W., Lüdtke, G., Konan, G., 1996. Two generations of Birimian (Paleoproterozoic) volcanic belts in northeastern Côte d'Ivoire (West Africa): consequences for the "Birimian controversy". Precambr. Res. 80, 173–191.
Hyndman, R.D., Vanyan, L.L., Marquis, G., Lawa, L.K., 1993. The origin of electrically conductive lower continental crust: saline water or graphite? Phys. Earth Planet. Inter. 81 (1–4), 325–345.
Jessell, M., Begg, G.C., Miller, M.S., 2016. The geophysical signatures of the West African Craton. Precambr. Res. 274, 3–24.
Jones, A.G., 1987. MT and reflection: an essential combination. Geophys. J. Roy. Astron. Soc. 89, 7–18.
Jones, A.G., 1992. The Continental Lower Crust, D.M. Fountain, R.J. Arculus, R.W. Kay (Eds.), Elsevier, New York, Ch. Electrical conductivity of the continental lower crust, pp. 81–143.
Jones, A.G., Jödicke, H., 1984. Magnetotelluric transfer function estimation improvement by a coherence-based rejection technique. 54th Ann. Mtg. Soc. of Expl. Geophys., Atlanta, Georgia.
Jones, A.G., Ferguson, I.J., Chave, A.D., Evans, R.L., McNeice, G.W., 2001. Electric lithosphere of the Slave craton. Geology 29, 423–426.
Khoza, D., Jones, A.G., Muller, M.R., Evans, R.L., Webb, S.J., Miensopust, M., the SAMTEX team, 2013. Tectonic model of the Limpopo belt: constraints from magnetotelluric data. Precambrian Res. 226.
Kiyan, D., Jones, A.G., Vozar, J., 2013. The inability of magnetotelluric off-diagonal impedance tensor elements to sense oblique conductors in three-dimensional inversion. Geophys. J. Int. 196, 1351–1364.
Kříbek, B., Sýkorová, I., Machovič, V., Laufek, F., 2008. Graphitization of organic matter and fluid-deposited graphite in Palaeoproterozoic (Birimian) black shales of the Kaya-Goren greenstone belt (Burkina Faso, West Africa). J. Metamorph. Geol. 26, 937–958.
Ledo, J., 2005. 2-D versus 3-D magnetotelluric data interpretation. Surv. Geophys. 26, 511–543.
Lemoine, S., 1990. Le faisceau d'accidents Greenville-Ferkessedougou-Bobo-Dioulasso (Libéria, Côte d'Ivoire, Burkina Faso); témoin d'une collision oblique éburnéenne. 15e colloque de géologie africaine. CIFEG, Paris, Nancy, France, 67–70.
Leube, A., Hirdes, W., Mauer, R., Kesse, G.O., 1990. The early Proterozoic Birimian Supergroup of Ghana and some aspects of its associated gold mineralization. Precambr. Res. 46, 139165.
Loh, G., Hirdes, W., 1996. Explanatory notes for the geological map of south-west Ghana 1:100 000-Sheets Sekondi (0402a) and Axim (0403b). Ghana Geol. Surv. Bull. 49 (63).
Lompo, M., 2010. Paleoproterozoic structural evolution of the Man-Leo Shield (West Africa) Key structures for vertical to transcurrent tectonics. J. Afr. Earth Sc. 58 (19–36).
Lüdtke, G., Hirdes, W., Konan, G., Koné, Y., N'da, D., Traoré, Y., Zamblé, Z., 1999. Géologie de la région Haute Comoé Sudfeuilles Dabakala (2b, d et 4b, d). Direction de la Géologie Abidjan Bulletin 176.
Mareschal, M., 1986. Modeling of natural source of magnetospheric origin in the interpretation of regional induction studies: a review. Surv. Geophys. 8, 261–300.
Metelka, V., Baratoux, L., Naba, S., Jessell, M.W., 2011. A geophysically constrained lithostructural analysis of the Eburnean greenstone belts and associated granitoid domains, western Burkina Faso. Precambr. Res. 190, 48–69.
Miensopust, M., Jones, A.G., Muller, M.R., Garcia, X., Evans, R.L., 2011. Lithospheric structures and Precambrian terrane boundaries in northeast-ern Botswana revealed through magnetotelluric profiling as part of the Southern African Magnetotelluric Experiment. J. Geophys. Res. Solid Earth 116 (B02401).
Muller, M.R., Jones, A.G., Evans, R.L., Grütter, H.S., Hatton, C., Garcia, X., Hamilton, M.P., Miensopust, M.P., Cole, P., Ngwisanyi, T., Hutchins, D., Fourie, C.J., Jelsma, H.A., Evans, S.F., Aravanis, T., Pettit, W., Webb, S.J., Wasborg, J., Team, The.X., 2009. Lithospheric structure, evolution and diamond prospectivity of the Rehoboth Terrane and western Kaapvaal Craton, southern Africa: constraints from broadband magnetotellurics. Lithos 112S, 93–105.
Pasyanos, M.E., Nyblade, A.A., 2007. A top to bottom lithospheric study of Africa and Arabia. Tectonophysics 444, 27–44.
Pons, J., Barbey, P., Dupuis, D., Leger, J.M., 1995. Mechanisms of plu-ton emplacement and structural evolution of a 2.1 Ga juvenile continental crust: the Birimian of southwestern Niger. Precambr. Res. 281–301.
Ritz, M., 1983. Use of the Magnetotelluric method for a better Understand-ing of the West Africa Shield. J. Geophys. Res. 88 (B12), 10625–10633.
Ritz, M., 1984. Inhomogeneous Structure of the Senegal Lithosphere From Deep Magnetotelluric Soundings. J. Geophys. Res. 89 (B13), 11317–11331.
Rooney, A.D., Selby, D., Houzay, J.-P., Renne, P.R., 2010. Re–Os geochronology of a Mesoproterozoic sedimentary succession, Taoudeni basin, Mauritania: implications for basin wide correlations and Re–Os organic-rich sediments systematic. Earth Planet. Sci. Lett. 289 (3–4), 486–496.
Rousseeuw, P.J., 1984. Least median of squares regression. J. Am. Statist. Assoc. 79, 871–880.
Schwartz, M.O., Melcher, F., 2003. The Perkoa zinc deposit, Burkina Faso. Econ. Geol. 98, 1463–1485.
Selway, K., Hand, M., Heinson, G.S., Payne, J.L., 2009. Magnetotelluric constraints on subduction polarity: reversing reconstruction models for Proterozoic Australia. Geology 37 (9), 799–802.
Sheriff, R.E., 1984, Encyclopedic dictionary of exploration geophysics (2nd ed.): Tulsa, OK, Society of Exploration Geophysicists, p. 323.
Siripunvaraporn, W., Egbert, G., Lenbury, Y., Uyeshima, M., 2005. Three-dimensional magnetotelluric inversion: data-space method. Phys. Planet. Interiors 150, 3–14.
Smirnov, M.Y., 2003. Magnetotelluric data processing with a robust statistical procedure having a high breakdown point. Geophys. J. Int. 152, 1–7.
Spratt, J.E., Jones, A.G., Jackson, V.A., Collins, L., Avdeeva, A., 2009. Lithospheric geometry of the Wopmay orogen from a Slave craton to Bear Province magnetotelluric transect. J. Geophys. Res. 114 (B01101).
Teal, D.J., Kah, L.C., 2005. Using C-isotopes to constrain interbasinal stratigraphic correlations, Mesoproterozoic Atar Group, Mauritania. Geol. Soc. Am. 37, 45 Abstracts with Programs.
Vidal, M., Gumiaux, C., Cagnard, F., Pouclet, A., Ouattara, G., Pichon, M., 2009. Evolution of a paleoproterozoic "weak type" orogeny in the West African Craton (Ivory Coast). Tectonophysics 477, 145159.
Wannamaker, P.E., 2000. Comment on "the petrologic case for a dry lower crust" by Bruce W. D. Yardley and John W. Valley. J. Geophys. Res. 105 (B3), 6057–6064.
Wei, W., Le Pape, F., Jones, A.G., Vozar, J., Dong, H., Unsworth, M.J., Jin, S., Ye, G., Jing, J., Zhang, L., Xie, C., 2014. Northward channel flow in northern Tibet revealed from 3D magnetotelluric modelling. Phys. Earth Planet. Inter. 235, 13–24.
Yardley, W.D., Valley, W., 1997. The petrologic case for a dry lower crust. J. Geophys. Res. 102, 12173–12185.
Yoshino, T., Noritake, F., 2011. Unstable graphite films on grain boundaries in crustal rocks. Earth Planet. Sci. Lett. 306, 186–192.